Tomography Images to Analyze the Deformation of the Cavern in the Continuous-Flow Mixing of Non-Newtonian Fluids

Dineshkumar Patel, Farhad Ein-Mozaffari, and Mehrab Mehrvar
Dept. of Chemical Engineering, Ryerson University, Toronto, ON M5B 2K3, Canada

DOI 10.1002/aic.14235
Published online October 2, 2013 in Wiley Online Library (wileyonlinelibrary.com)

Tomography, an efficient nonintrusive technique, was employed to visualize the flow in continuous-flow mixing and to measure the cavern volume (V_c) in batch mixing. This study has demonstrated an efficient method for flow visualization in the continuous-flow mixing of opaque fluids using two-dimensional (2-D) and 3-D tomograms. The main objective of this study was to explore the effects of four inlet-outlet configurations, fluid rheology (0.5–1.5% xanthan gum concentration), high-velocity jet (0.317–1.660 m s^{-1}), and feed flow rate (5.3×10^{-5}–2.36×10^{-4} m^3 s^{-1}) on the deformation of the cavern. Dynamic tests were also performed to estimate the fully mixed volume ($V_{fully\ mixed}$) for the RT, A310, and 3AM impellers in a continuous-flow mixing system, and it was found that $V_{fully\ mixed}$ was greater than V_c. Incorporating the findings of this study into the design criteria will minimize the extent of nonideal flows in the continuous-flow mixing of complex fluids and eventually improve the quality of end-products. © 2013 American Institute of Chemical Engineers
AIChE J, 60: 315–331, 2014

Keywords: mixing, non-Newtonian fluids, tomography, cavern, flow visualization

Introduction

The key objective of any mixing process is to maximize the degree of homogeneity of a property such as concentration, viscosity, color, and temperature. One of the most common operations encountered in the chemical and allied process industries is the mixing in stirred vessels. These industries frequently encounter non-Newtonian fluids with yield stress such as pulp suspensions, certain polymer and biopolymer solutions, and wastewater sludge. Due to the complex rheology of non-Newtonian fluids, the design of mixing systems for these types of fluids is more challenging than that for the Newtonian fluids. Mixing of yield stress fluids leads to the formation of a well-mixed zone around the impeller (cavern) surrounded by a stagnant zone far from the impeller, where the impeller-imparted shear stress fails to exceed fluid yield stress.[1] The existence of stagnant regions within a mixing vessel leads to ineffective heat and mass transfer, which results in the poor quality of end products, product degradation, and production loss. To improve the mixing efficiency of a reactor, it is always beneficial to eradicate such undesired stagnant zones in the mixing of non-Newtonian fluids with yield stress.

Some researchers have developed models to predict the cavern size as a function of mixing conditions and fluid properties. Solomon et al.[2] assumed a spherical cavern with the torque induced by the impeller acting tangentially at the cavern boundary. Subsequently, Elson and Cheesman[3] and Elson[4] proposed a cylindrical model, which effectively predicted the behavior of the cavern before it reached the vessel walls. This proposed model (Eq. 1) specifies that the dimensionless cavern diameter (D_c/D) is proportional to the product of the power (P_o) and the yield stress Reynolds number (Re_y)

$$\left(\frac{D_c}{D}\right)^3 = \left(\frac{1}{\left({}^{H_c}/_{D_c} + 1/3\right)\pi^2}\right)\left(\frac{N^2 D^2 \rho}{\tau_y}\right) P_0 \qquad (1)$$

where D_c, D, H_c, N, ρ, and τ_y are the cavern diameter, impeller diameter, cavern height, impeller rotational speed, fluid density, and fluid yield stress, respectively. The term $N^2D^2\rho/\tau_y$ on the right hand side of Eq. 1 is referred to as the yield stress Reynolds number, Re_y. Amanullah et al.[5] developed an axial force model for a torus-shaped cavern, whereas Wilkens et al.[6] proposed a model for an elliptical torus-shaped cavern without accounting the axial force. Hirata and Aoshima[7] also suggested a model based on viscous dissipation for a cylindrical-shaped cavern. Hui et al.[8] developed an axial force cavern model, which accounted for interaction between the cavern and vessel walls due to the impeller location. Amanullah et al.[5] showed that the cylindrical model represents the cavern shape better than the spherical model. In fact, the cylindrical model (Eq. 1) has been widely used to measure the cavern size.[9,10]

Studying continuous-flow mixing is more challenging than studying the batch mixing due to the additional operating conditions and design parameters such as inlet and outlet locations, and the feed flow rate. The studies on yield stress fluids have shown that nonideal flows such as channeling, recirculation, and dead volumes significantly affect the performance of continuous-flow mixing systems.[11] To improve the efficiency of continuous-flow mixing systems, these

Correspondence concerning this article should be addressed to F. Ein-Mozaffari at fmozaffa@ryerson.ca.

nonideal flows should be minimized in stirred vessels. Using laser Doppler velocimetry, Mavros et al.[12–14] studied continuous-flow mixing of Newtonian fluids and found that nonideal flows such as channeling are likely to occur in a mixer if the ratio of residence time to batch mixing time is less than 10. Using the spectrophotometer, Roussinova and Kresta[15] studied the continuous-flow mixing of Newtonian fluids and found that for the design of an ideal mixer, a line from the inlet to the outlet should pass through the impeller. Using residence time distribution (RTD) and computational fluid dynamics (CFD), Samaras et al.[16] studied the continuous-flow mixing of Newtonian fluids. They revealed that mixing Newtonian fluids with axial-flow impellers was prone to channeling when the location of the outlet was directly below the impeller discharge; however, such a potential problem was not observed when a radial-flow impeller was used. Using CFD, Aubin et al.[17] studied the effects of pumping directions of an axial flow impeller in the continuous-flow mixing of Newtonian fluids. They observed that the channeling through a bottom outlet (BO) may be reduced when the impeller was employed in the up-pumping mode instead of the down-pumping mode. Using CFD, Khopkar et al.[18] simulated the fluid flow of the continuous-flow mixing of Newtonian fluids and found that the locations of the inlet and outlet affect the performance of continuous-flow mixing systems. All these studies were conducted for the Newtonian fluids.

Using CFD, Ford et al.[19] simulated the fluid flow of pulp suspensions, a non-Newtonian fluid, in an agitated pulp stock chest equipped with a side-entering impeller. It was observed that the extent of nonideal flows was reduced using the BO compared to the side outlet while providing the inlet at the top of the vessel. Using dynamic tests, Patel et al.[20] and Ein-Mozaffari et al.[21] studied the effect of impeller size on the performance of the continuous-flow mixing of non-Newtonian fluids with yield stress. They found that the efficiency of the continuous-flow mixer improved as the impeller diameter was increased. The fluid feed flow rate[22] and fluid rheology[23] also affect the performance of a continuous-flow mixing system. The dynamic test results showed that the extent of nonideal flows such as channeling and dead volume increased when the fluid yield stress as well as the feed flow rate were increased in the mixing of non-Newtonian fluids exhibiting yield stress.[24,25] Using dynamic tests, Patel et al.[20] also explored the effect of fluid height in the vessel, types of impellers (axial-flow and radial-flow), impeller off-bottom clearance, residence time, and jet velocity on the dynamic performance of the continuous-flow mixing of non-Newtonian fluids. They found that as the fluid height in the vessel was increased, the extent of nonideal flows also increased while increasing the residence time of the fluid in the vessel decreased the effect of nonideal flows. Moreover, the extent of nonideal flows decreased when the clearance of the impeller was increased from $H/3.4$ to $H/2.1$ and the jet velocity was increased from 0.317 to 1.66 m s^{-1}. Using electrical resistance tomography (ERT) and dynamic tests, Patel et al.[26] characterized the continuous-flow mixing of non-Newtonian fluids possessing yield stress using the ratio of residence time to the batch mixing time. The results showed that the nonideal flows are likely to occur in the continuous-flow mixing system, if this ratio is less than 8.2.

A comprehensive literature review reveals that most of these studies have been carried out for the continuous-flow mixing of Newtonian fluids and very few researchers have explored the continuous-flow mixing of pseudoplastic fluids exhibiting yield stress. Moreover, most of these investigators have utilized CFD and RTD. Based on the authors' knowledge, no study has employed the tomography technique to study the effect of the input-output flow on the performance of the continuous-flow mixing of non-Newtonian fluids with yield stress in a stirred vessel. Furthermore, no study has been attempted to relate the volume of the cavern in the batch mode to the fully mixed volume in the continuous-flow mode. Therefore, the objectives of this research were to explore the effect of the inlet and outlet locations, fluid rheology, feed jet velocity, and feed flow rate on the deformation of the cavern generated in the mixing of pseudoplastic fluids possessing yield stress in a stirred vessel and to visualize the flow in two-dimensional (2-D) and 3-D using tomography images. In addition, the distinction between the cavern volume measured by ERT in a batch vessel and the fully mixed volume obtained through dynamic tests in a continuous-flow vessel was noticeably identified for the axial-flow and radial-flow impellers.

Experimental Setup and Procedure

A mixing system (Figure 1) used in this study consists of a transparent flat-bottomed cylindrical tank with a diameter (T) of 0.38 m and a height of 0.60 m. The tank was equipped with four equally spaced baffles with a width of $T/10$. Six tomography sensor planes were positioned around the circumference of the mixing tank. The planes were 0.06 m apart from each other with the bottom plane 0.04 m from the bottom of the tank. The planes were numbered from top ($P1$) to bottom ($P6$). Each plane had 16 stainless steel electrodes which were located equidistantly on the periphery of the vessel. The height, width, and thickness of the electrodes were 0.02, 0.03, and 0.001 m, respectively. Each electrode was in direct contact with the working fluid in the tank without invading the flow and was connected to the ERT system (Industrial Tomography Systems, Manchester, UK). The tomography machine was connected to a computer for the image reconstruction. The fluid height (H) in the tank was 0.41 m providing a total volume around 0.047 m^3. The axial-flow impellers (A310 and 3AM) and the radial-flow impeller (RT), each with a 0.18 m diameter (D), were utilized to stir xanthan gum solutions (Figure 1). The 3AM impeller (Hayward Gordon Ltd.) is a three-blade hydrofoil impeller with a medium solidity ratio. The impeller was located on plane $P4$ with an off-bottom clearance of 0.16 m. The mixing tank was equipped with a top-entering impeller driven by a 2-hp motor, and the impeller speed was set to the desired revolution per minute (rpm) using a variable frequency drive. The impeller torque and speed were measured using a rotary torque transducer (Staiger Mohilo, Lorch, Germany) and a tachometer, respectively. The diameters of the inlet and outlet pipes were 0.025 m. To investigate the effect of inlet and outlet locations on the performance of continuous-flow mixing, the inlets were located at the top ($r = 0.13$ m, $\Phi = 90^\circ$, and $z = 0.38$ m) and at the bottom ($r = 0.05$ m, $\Phi = 105^\circ$, and $z = 0.10$ m) of the mixing vessel. Similarly, the outlets were located at the bottom ($r = 0.13$ m, $\Phi = 315^\circ$, and $z = 0.00$ m) and side ($r = 0.19$ m, $\Phi = 315^\circ$, and $z = 0.35$ m) of the mixing vessel.

To measure the cavern size in the batch mode, 3×10^{-5} m^3 of 5% saline solution (tracer) was injected directly into the xanthan gum solution near the impeller hub using a

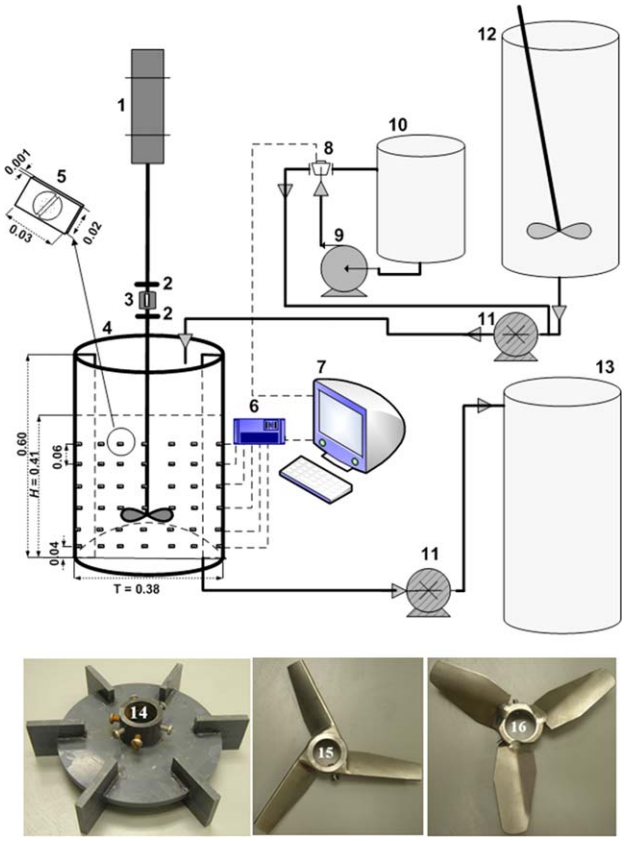

Figure 1. Experimental set-up (dimensions in m): (1) electric motor, (2) flexible coupling, (3) torque meter, (4) mixing tank, (5) electrode, (6) ERT data acquisition system (7) host computer, (8) solenoid valve, (9) metering pump, (10) tracer tank, (11) progressive cavity pump, (12) feed tank, (13) discharge tank, (14) RT (Rushton turbine), (15) Lightnin A310, and (16) Hayward Gordon 3AM.

[Color figure can be viewed in the online issue, which is available at wileyonlinelibrary.com.]

plastic syringe and the tracer concentration was monitored using ERT. Before the injection of the tracer, the reference state was taken to eliminate the effect of the stirrer and other internals within the mixing tank. Measurements were collected from six planes of electrodes until the cavern size remained unchanged. Then tomography images were used to measure the cavern diameter (D_c), cavern height (H_c), and cavern volume (V_c) generated around the impeller. It should be mentioned that the diffusion of the saline solution into the static non-Newtonian fluid region is negligible due to the high apparent viscosity of the xanthan gum solution at the shear stresses less than the yield stress and it could not significantly affect the measurement of the cavern size during 30 s of each test in the batch mode. To visualize the flow in the continuous-flow mixing system using ERT, once the cavern was fully developed, the feed and discharge pumps were turned on simultaneously while the impeller was still running at the given speed and the fluid was pumped from the feed tank to the discharge tank through the mixing vessel. ERT data were collected, and tomography images were reconstructed to visualize the flow inside the mixing vessel. To measure the fully mixed volume ($V_{\text{fully mixed}}$) in the continuous-flow mixing system through the dynamic test, the system was excited by injecting the saline solution into the fresh feed stream prior to being pumped into the mixing vessel using a metering pump (Milton Roy, USA). The saline solution was injected into the feed stream at the suction of the feed pump. Thus, it was premixed with the xanthan gum solution before entering into the mixing vessel. The tracer was injected by a computer-controlled on-off solenoid valve (Ascolectric, Canada). The conductivity values of input and output streams were measured as a function of time using flow-through conductivity sensors (RoseMount Analytical, Irvine, CA) and were recorded using a data acquisition system (DAS) controlled by LabVIEW software (National Instruments, Austin, TX). Thermocouples were installed at the inlet and outlet of the mixing vessel to measure the fluid temperature. All measurements were made at room temperature 22 ± 1°C. To quantify the extent of nonideal flows in the continuous-flow mixing vessel, the dynamic model (Eq. 2) proposed by Ein-Mozaffari et al.[27] was used in this study

$$G = \frac{fe^{-T_1 s}}{1+\tau_1 s} + \frac{(1-f)(1-R)\frac{e^{-T_2 s}}{1+\tau_2 s}}{1-\frac{R\ e^{-T_2 s}}{1+\tau_2 s}} \tag{2}$$

where G is the transfer function for the system in a continuous-time domain, and parameters τ_1 and τ_2 are the time constants for the channeling and mixing zones, respectively. Parameters T_1 and T_2 are the time delays for the channeling and mixing zones, respectively. Parameter f represents the portion of the fluid channelled in the mixing tank, and $1-f$ is the fraction of the fluid entered in the mixing zone. A portion of the fluid, R, exiting the mixing zone can be recirculated within the mixing zone. The fully mixed volume in a mixing vessel was calculated by[27]

$$\frac{V_{\text{fully mixed}}}{V_{\text{total}}} = \frac{Q\tau_2(1-f)}{V_{\text{total}}} \tag{3}$$

where $V_{\text{fully mixed}}$ is the fully mixed volume in the vessel, V_{total} is the total solution volume in the vessel, and Q is the feed flow rate through the mixing vessel. It must be mentioned that the nominal fully mixed volume is calculated using $V_{\text{fully mixed}} = \tau Q$, where τ and Q are the nominal residence time and total feed flow rate, respectively. However, this equation cannot be used for the continuous-flow mixing of non-Newtonian fluids as the nonideal flows exist within the mixing tank. Thus, to calculate the actual fully mixed volume, we should employ the residence time of the mixing zone (τ_2) and the fraction of the feed, which enters to the mixing zone. Since f is the fraction of the feed, which is short-circuited, the flow rate to the mixing zone would be $Q(1-f)$. Therefore, the actual fully mixed volume is calculated using $V_{\text{fully mixed}} = Q(1-f)\ \tau_2$. By measuring the input and output responses of the mixing vessel, the dynamic model (Eq. 2) parameters were estimated using the numerical method developed by Kammer et al.[28] The identification experiment was performed through exciting the system with a frequency-modulated random binary signal and examining the input and output conductivities over a precise time interval.[29]

The system identification procedure comprised the following steps:[28,29] (1) exciting the system with a rectangular pulse, (2) designing a frequency-modulated random binary signal on the basis of the response of the system to the

Table 1. Experimental Conditions

Descriptions	Range and Types
Impeller types	Axial-flow impeller: A310 and 3AM Radial-flow impeller: RT
Impeller speed (N)	22–127 rpm
Fluid rheology (RT impeller)	0.5, 1.0, and 1.5 wt/v % xanthan gum solution
Fluid flow rate (Q) (RT impeller)	5.3×10^{-5}, 1.60×10^{-4}, and 2.36×10^{-4} m^3 s^{-1}
Jet velocity (V_j) (RT impeller)	0.317 and 1.66 m s^{-1}
Inlet locations (RT impeller)	TI ($r = 0.13$ m, $\Phi = 90^\circ$, and $z = 0.38$ m) BI ($r = 0.05$ m, $\Phi = 105^\circ$, and $z = 0.10$ m)
Outlet locations (RT impeller)	TO ($r = 0.19$ m, $\Phi = 315^\circ$, and $z = 0.35$ m) BO ($r = 0.13$ m, $\Phi = 315^\circ$, and $z = 0.00$ m)

rectangular pulse by concentrating the excitation energy at frequencies where the Bode plot is sensitive to the parameters' variations, (3) exciting the system by a frequency-modulated random binary signal, and (4) validating the dynamic model with a new input imposed by another random exciting signal to generate a new output and then comparing the measured and predicted outputs. The system was excited with the frequency-modulated random binary signal using the LabVIEW software. The signals were sent to the solenoid valve, which controlled the injection of the saline solution into the feed stream.

Xanthan gum solutions in water with 0.5, 1.0, and 1.5% mass concentration were used in this study. Xanthan gum solution is a shear-thinning fluid possessing yield stress and its rheological properties can be described by the Herschel–Bulkley model[30]

$$\tau_s = \tau_y + K(\dot{\gamma})^n \tag{4}$$

where τ_s is the shear stress, τ_y is the yield stress, K is the consistency index, $\dot{\gamma}$ is the shear rate, and n is the power-law index. The rheological properties of the xanthan gum solutions can be found in Saeed et al.[10] The experimental conditions for batch and continuous modes are summarized in Table 1.

X-ray and gamma-ray tomography techniques have been employed to explore the gas-liquid mixing in stirred tank reactors.[31–34] ERT has been used in various chemical engineering processes such as, to name a few, solid-liquid mixing,[35,36] and non-Newtonian fluid mixing.[9,37] In this study, ERT was used to measure the cavern size and analyze the fluid flow in 2-D and 3-D domains. The sensing, data acquisition, and image reconstruction are the principal elements of the ERT system. The electrodes, which were located around the boundary of the vessel, made the electrical contact with the fluid inside the vessel and were connected to the DAS. Because the adjacent strategy demands less hardware and provides fast image reconstruction, it was used in this study. In this strategy, current is applied through a pair of two adjacent electrodes and voltage is measured at the remaining adjacent pairs of electrodes, and the injection pair is switched to the next pair of electrodes and the voltages for all other electrode pairs are measured. This process is then repeated until all possible combinations are tried. In this study, each plane had 16 stainless steel electrodes located on the periphery of the vessel. Thus, this strategy provided 104 individual voltage measurements according to the equation $n_e(n_e - 3)/2$ where n_e is the number of electrodes per plane.[38] The six tomography sensor planes provided 624 voltage measurements. Eventually, the DAS communicated these quantitative data to the host image reconstruction computer, where the data were processed using a suitable image reconstruction algorithm. In this study, the linear back projection algorithm,[39] which is a noniterative algorithm, was used to convert raw voltage measurements into a 2-D conductivity map of the each plane because the iterative algorithm is often computationally more time consuming and too slow for the real-time image reconstruction compared to the noniterative algorithm. To calculate the conductivity distribution, the area of the interest is usually gridded spatially to equal squares. Each individual tomogram consists of a 20 × 20 pixel array giving 400 spatial elements. However, some of these pixels lie outside the vessel circumference and the image is formed from the pixels inside the vessel. The circular image is constructed using 316 pixels. Because the mixing vessel had six sensing planes, this produced 1896 nonintrusive conductivity probes.

Results and Discussion

The power consumption plays a significant role in the assessment of the mixing performances of the impellers. The power (P) consumed by the impellers was calculated using $P = 2\pi NM$, where N and M were the impeller rotational speed and the torque, respectively. The friction torque was subtracted from the torque measured for the impeller rotating in the mixing vessel with fluid. The power number (P_o) was then calculated using $P_o = P/\rho D^5 N^3$, where D and ρ were impeller diameter and the fluid density, respectively. The average shear rate ($\dot{\gamma}_{avg}$) obtained from the Metzner and Otto's correlation[40] ($\dot{\gamma}_{avg} = k_S N$, where k_S is a function of the type of the impeller) was used to evaluate the apparent viscosity (η) of the Herschel–Bulkley fluid. The modified Reynolds number (Re) for this type of fluid was calculated as follows

$$Re = \frac{\rho N D^2}{\eta} = \frac{k_S \rho N^2 D^2}{\tau_y + K(k_S N)^n} \tag{5}$$

The value of k_S was set at 10 and 11.5 for axial-flow and radial-flow impellers, respectively.[26] The power number curves for the RT, A310, and 3AM impellers are depicted in Figure 2. The trend of the power number curve is similar to that reported in the literature.[41] The results show that at a Reynolds number less than 10, the solid line with a slope of

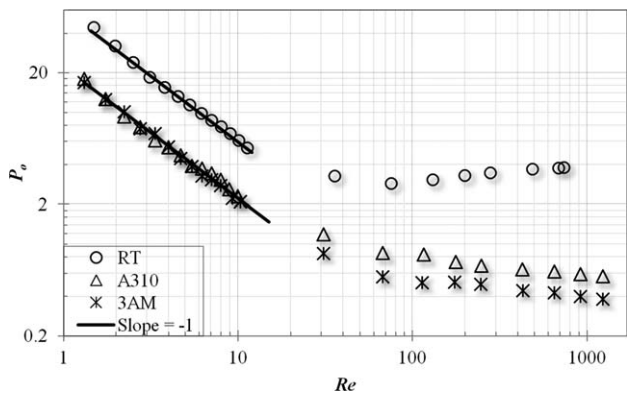

Figure 2. Power curves for the RT, A310, and 3AM impellers.

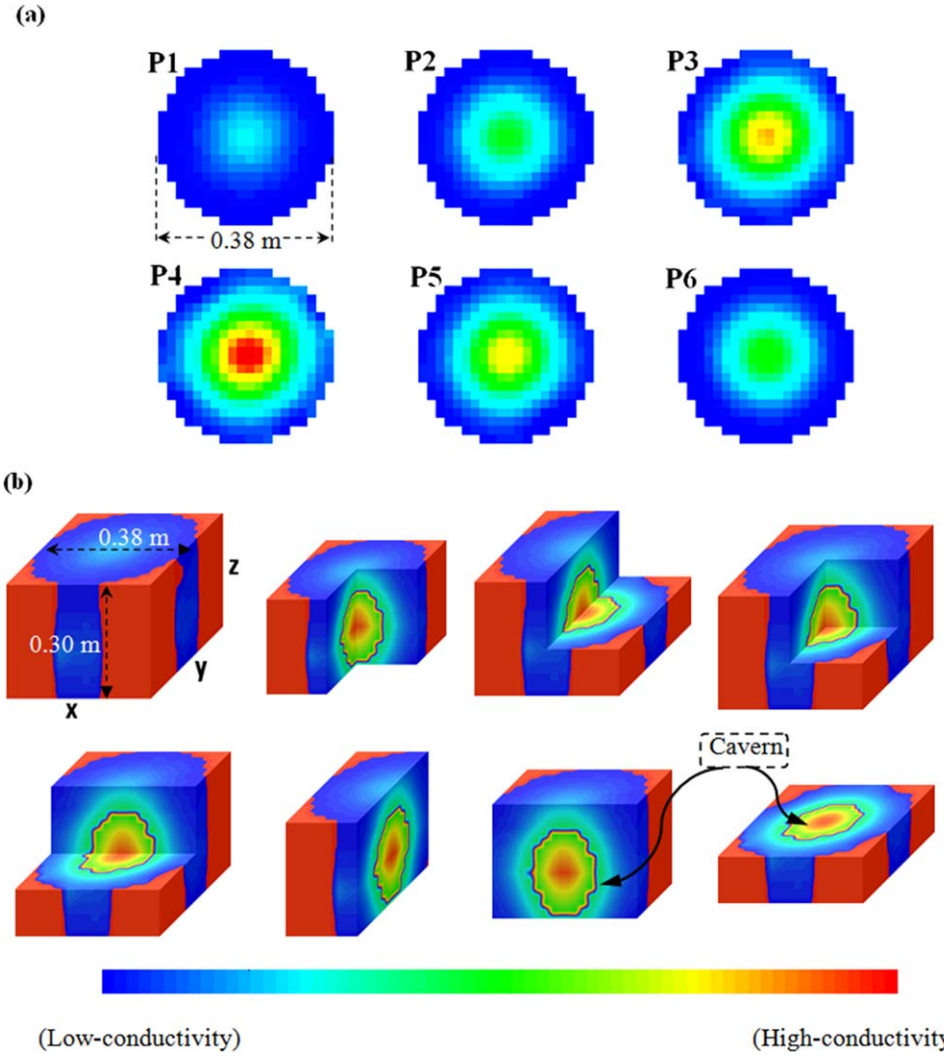

Figure 3. The 3-D images generated from the 2-D tomograms show the formation of the cavern in the mixing of the 0.5% xanthan gum solution using the RT impeller: (a) 2-D tomogram and (b) 3-D images generated using the Slicer Dicer software (the 3-D images were generated by cutting the vertical plane at the center of the tank and/or the horizontal plane on the impeller surface).

[Color figure can be viewed in the online issue, which is available at wileyonlinelibrary.com.]

-1 fitted the data precisely, which means that P_oRe was constant and the flow was in the laminar region. Moreover, in the transition region, P_o changed slightly with Re. The impeller power numbers found in this study (RT: 3.82; A310: 0.57; and 3AM: 0.38) are in the transition regime and within the range reported in the literature.[42]

The motion of pseudoplastic fluids possessing yield stress ceases when shear stresses are below the yield stress, which leads to the formation of a well-mixed zone around the impeller called the cavern. Figure 3a shows the formation of the cavern visualized using the 2-D tomograms generated after the injection of the tracer in the mixing of the 0.5% xanthan gum solution using the RT impeller. As shown in this figure, the impeller was located on the plane $P4$. The tracer was injected on the impeller plane near the impeller hub using a syringe. Colors in tomograms display the dispersion of the tracer in the vessel. The blue color in these tomograms demonstrates the low-conductivity zones and represents the lower tracer concentrations. The red color in the tomograms shows the high-conductivity regions and indicates the higher tracer concentration in those zones. At the boundary of the cavern, the conductivity of the fluid was equal to the conductivity of the fresh xanthan gum solution which was not zero but was lower than the conductivity of the solution containing salt. The conductivity of the fresh xanthan gum solution was about 0.9 mS. The 2-D tomogram shows that the tracer injected near the impeller hub remained within the cavern and no tracer was found in the surroundings. The spatial resolution of the ERT system is about 5% of the vessel diameter. This has been investigated through the phantom detection tests conducted by Holden et al.[43] Although the 2-D tomogram provides good images of the cavern formation, it is difficult to measure the cavern height using the 2-D tomogram. Therefore, 2-D images were converted into 3-D images. Figure 3b shows the 3-D images generated from the 2-D images using Slicer-Dicer software (PIXOTEC, USA). Based on the 3-D images, the shape of the cavern was approximated by a right circular cylinder; therefore, the characteristics of the cavern can be described by the diameter and height of this region. The cavern diameter was measured on a horizontal plane passing through the impeller on plane $P4$. The cavern height was measured on a

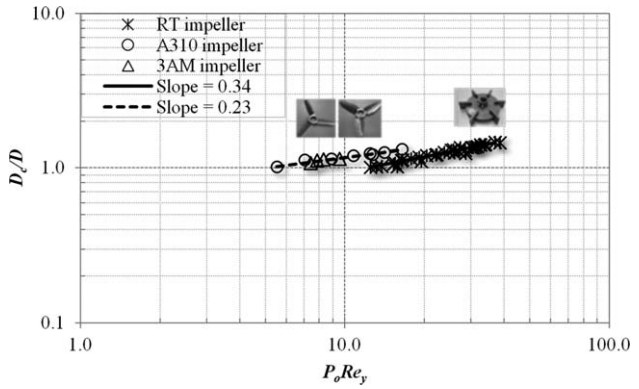

Figure 4. Dimensionless cavern diameter (Dc/D) vs. dimensionless P_oRe_y for the radial-flow impeller (RT) and axial-flow impellers (A310 and 3AM).

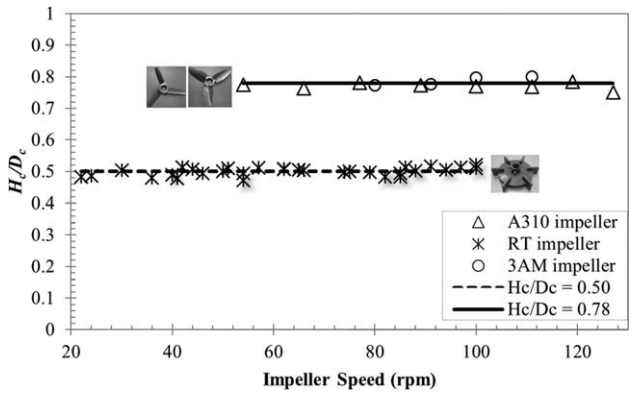

Figure 5. Dimensionless cavern height (H_c/D_c) vs. impeller speed (N) for the radial-flow impeller (RT) and axial-flow impellers (A310 and 3AM).

vertical plane along the shaft and perpendicular to the horizontal plane of the impeller. To visualize meticulously how the tracer was dispersed in the opaque fluid (xanthan gum solutions), 3-D images were generated by cutting the block in all possible ways on the x, y, and z axes to provide enough information about the cavern. Various 3-D images shown in Figure 3b were generated by cutting the vertical plane at the center of the tank and/or cutting a horizontal plane passing through the impeller on plane $P4$. The outlines around the cavern volume in Figure 3b were generated by the Slicer Dicer software in the default setting. Thus, the 3-D images provided a motivating insight to visualize the flow in the mixing of opaque fluids.

The measured cavern diameter was compared to those predicted using Elson's cylindrical model (Eq. 1). This model can be used to estimate the cavern diameter before the cavern touches the vessel wall. Figure 4 shows the dimensionless diameter (D_c/D) versus dimensionless P_oRe_y on a log-log scale for the RT impeller and two axial-flow impellers (A310 and 3AM). The diameter of the cavern was found to increase with an increase in the impeller speed and it continued to grow until the cavern reached the vessel wall. According to Elson's cylindrical model (Eq. 1), a log-log plot of the D_c/D versus P_oRe_y should give a slope of 1/3. As shown in Figure 4, the slope of this line calculated using the least-square method was 0.34 for the RT impeller. However, the slope of the D_c/D vs. P_oRe_y for the axial-flow impellers was 0.23, which was lower than that expected from Elson's cylindrical model. Galindo and Nienow[44] reported a value of 0.25 for the slope of the D_c/D vs. P_oRe_y for the A315 axial-flow impeller and Saeed et al.[10] reported a value of 0.24 for the A200, A100, and A310 axial-flow impellers. Thus, the results found in this study agreed well with the value reported in the open literature. In this study, the slope of the D_c/D vs. P_oRe_y line was found to be lower for the axial-flow impeller than that of the RT impeller (a radial-flow impeller). It means that a radial-flow impeller can provide a larger cavern diameter compared to an axial-flow impeller. This is due to the nature of impellers, as radial-flow impellers discharge fluid radially outward to the vessel wall, whereas axial-flow impellers discharge fluid axially along the shaft. Moreover, the radial-flow impellers provide a higher shear level with lower pumping compared to the hydrofoil impellers (A310 and 3AM).

In addition to the cavern diameter, the cavern height (H_c) was measured on a vertical plane along the shaft and perpendicular to the horizontal plane of the impeller. Figure 5 demonstrates the dimensionless cavern height (H_c/D_c) vs. the impeller speed (N) for the RT impeller and two axial-flow impellers (A310 and 3AM). It can be seen that before the cavern touched the wall, the ratio H_c/D_c was almost constant at 0.50 for the RT impeller. The value of this ratio is equal to the value reported by Hirata and Aoshima.[7] It can be also seen that the cavern height to cavern diameter ratio was constant at 0.78 for both axial-flow impellers. Saeed et al.[10] reported that the H_c/D_c was constant at 0.80 for the A310 impeller (axial-flow impeller). The results were in good agreement with those reported in the literature. The results clearly demonstrate that the caverns generated by the axial-flow impellers are taller than those of the radial-flow impeller. This is due to the fact that the axial-flow impellers discharge fluid axially along the shaft, whereas the radial-flow impellers discharge fluid radially outward to the vessel wall. Elson[4] also reported that the H_c/D_c ratio was higher for the axial-flow impellers (pitched blade turbine and paddle) than for the radial-flow impeller (disc turbine).

The cavern volume (V_c) was calculated using the cavern diameter (D_c) and the cavern height (H_c) for a cylindrical shape. Figure 6 represents the effect of fluid rheology on the dimensionless cavern volume (V_c/V_{total}) vs. the power per unit volume for the RT impeller at 0.5, 1.0, and 1.5%

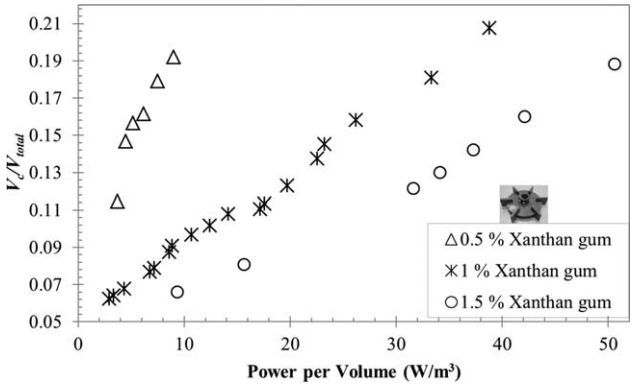

Figure 6. Effect of the fluid rheology on the dimensionless cavern volume for the RT impeller at 0.5, 1.0, and 1.5 % xanthan gum solutions.

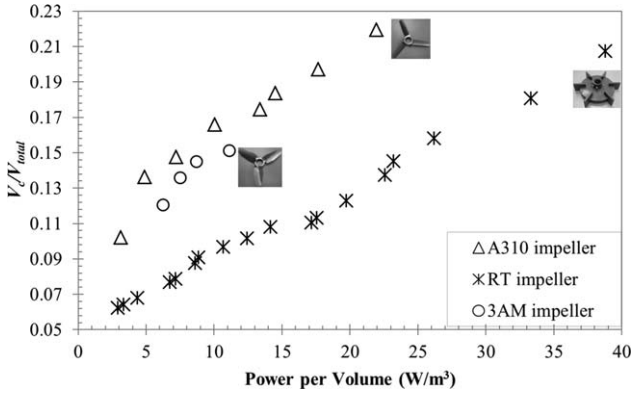

Figure 7. Effect of the impeller type on the dimensionless cavern volume (A310, RT, and 3AM impellers and 1.0 % xanthan gum solution).

xanthan gum solutions in the batch mode. The results show that as the impeller speed/power was increased, the cavern diameter and height also increased for all concentrations and so did the cavern volume (V_c). However, with respect to the xanthan gum concentration, the dimensionless cavern volume (V_c/V_{total}) was observed as decreasing. This can be attributed to the effect of the yield stress, which increases with the xanthan gum concentrations. More stagnant regions are formed in the mixing vessel where shear stress fails to exceed yield stress, which reduces the cavern volume. Therefore, the dimensionless cavern volume decreased with an increase in the xanthan gum concentrations. Similarly, the cavern volume was calculated for the axial-flow impellers as well. Figure 7 demonstrates how impeller types (axial-flow and radial-flow) influenced the dimensionless cavern volumes at 1.0% xanthan gum solution in the batch mode. It can be seen that for given operating conditions, the hydrofoil impellers (A310 and 3AM) were more efficient than the radial-flow impeller (RT) in generating a larger cavern. Similar results were found by Amanullah et al.[45] who showed that the axial-flow impeller produced larger cavern volumes for a given power input than the radial-flow impeller. It should be mentioned that although both axial-flow and radial-flow impellers are designed for the transitional and turbulent flow applications, the hydrofoil impellers (A310 and 3AM) can provide a high axial-flow at a reduced shear. They are also more efficient and are capable of more streamlined pumping. Compared to the axial-flow impellers, the radial-flow impellers provide a higher shear and turbulence level with lower pumping.[41]

To compare the cavern volume (V_c) in the batch vessel with the fully mixed volume ($V_{\text{fully mixed}}$) in the continuous-flow mixing system, dynamic tests were also performed for the axial-flow impellers (A310 and 3AM) and the radial-flow impeller (RT) agitated in 1% xanthan gum solution. In these experiments, ERT tests in the batch mode and dynamic tests in the continuous-flow mode were conducted with the identical operating conditions except for the feed flow rate ($Q = 1.60 \times 10^{-4}$ m^3 s^{-1}; residence time = 292 s) and the location of the inlet and outlet, which were additional to the continuous-flow mode. The comparisons between the dimensionless cavern volume (V_c/V_{total}) in the batch mode and the fraction of the fully mixed volume ($V_{\text{fully mixed}}/V_{\text{total}}$) in the continuous-flow mode for the RT, A310, and 3AM impellers are depicted in Figures 8a–c, respectively. From the results,

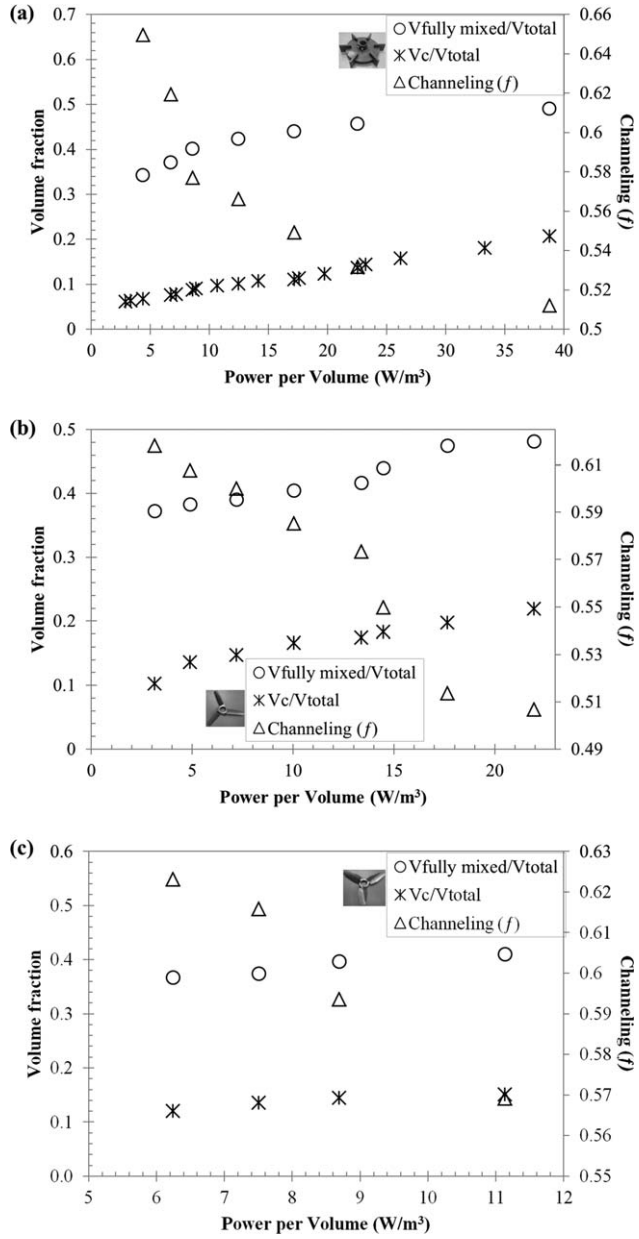

Figure 8. Dimensionless cavern volume (V_c/V_{total}), the fraction of fully mixed volume ($V_{\text{fully mixed}}/V_{\text{total}}$), and the extent of channeling (f) as a function of the specific power at 1% xanthan gum solution for the (a) RT impeller, (b) A310 impeller, and (c) 3AM impeller.

it can be clearly seen that the fully mixed volume generated in the continuous-flow mixing system was higher than the cavern volume generated in the batch mixing system for all three (RT, A310, and 3AM) impellers with the given operating conditions. This can be attributed to the momentum added to the fluid in the mixing vessel by the input and output flows passing through the vessel. Mixing of the fluid requires the input of mechanical energy to achieve the process results. In both the batch and continuous-flow modes, this energy is generally provided through the impeller. An alternative method for getting energy into the fluid is to generate a jet stream of fluid in the vessel. This jet entrains and mixes the surrounding fluids, and the mechanical energy is

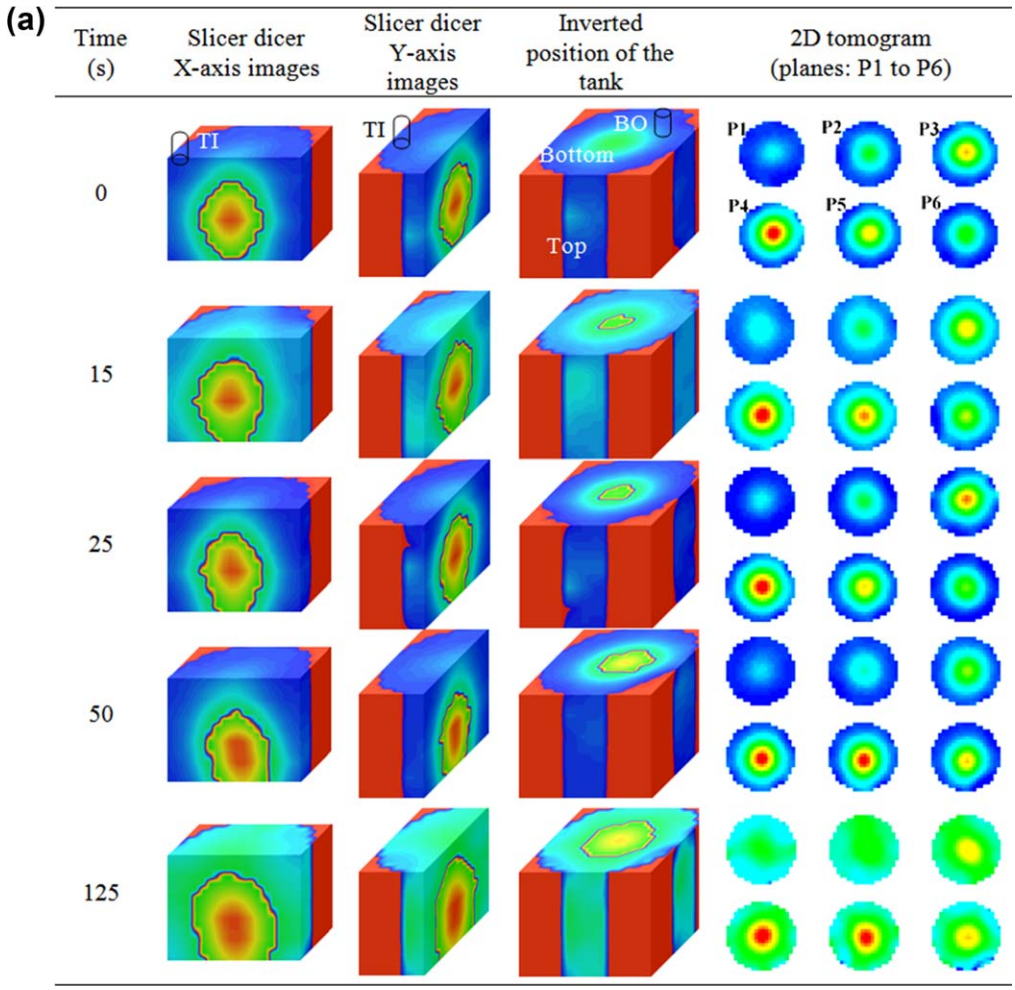

Figure 9. Effect of inlet and outlet locations on the deformation of the cavern for four different configurations: (a) TI-BO, (b) BI-BO, (c) TI-TO, and (d) BI-TO (RT impeller, $N = 30$ rpm, $Q = 1.60 \times 10^{-4}$ m^3 s^{-1}, 1.0% xanthan gum, and $V_j = 0.317$ m s^{-1}).

[Color figure can be viewed in the online issue, which is available at wileyonlinelibrary.com.]

supplied from a pump.[41] This is achieved through the feed stream in the continuous-flow mode. In fact, in the continuous-flow mixing system the fluid passing from the inlet to the outlet generates extra flows and adds more momentum to the fluid flow in the stirred vessel. The extra momentum flux ($Q\ \rho\ v/A$, where v is the velocity of the fluid passing through the inlet, and A is the cross section area of the inlet pipe) added to the fluid in the mixing vessel at the inlet position was about 99.92 Kg m^{-1} s^{-2}. Due to this fact, the size of the mixed volume in the continuous mode was higher than that in the batch mode. It is very clear from the images shown in Figure 9a that the size of the cavern increased as the flow passed through the mixing tank. These images are discussed in detail in the subsequent paragraph where the ERT flow visualization results are described. Furthermore, the momentum flux generated due to the inlet-outlet flow was compared with the momentum flux generated by the impeller. The impeller pumping rate (Q_{impeller}) is defined as $Q_{\text{impeller}} = N_Q N D^3$, where N_Q is the impeller flow number.[46] N_Q for the A310 impeller was obtained from the literature.[47] The momentum flux ($Q_{\text{impeller}}\ \rho\ v_{\text{tip}}/A_i$, where v_{tip} is the impeller tip velocity, and A_i is the swept area by the impeller) generated by the A310 impeller at $N = 30$ rpm was estimated at about 1.57 Kg m^{-1} s^{-2}, which was almost 63.5 times lower than the momentum flux generated by the inlet flow (99.92 Kg m^{-1} s^{-2}). The momentum flux generated by the A310 impeller at $N = 100$ rpm was about 73.32 Kg m^{-1} s^{-2}, which was approximately 1.3 times lower than the momentum flux generated by the inlet flow (99.92 Kg m^{-1} s^{-2}). Thus, these results demonstrate that at a lower impeller speed, the momentum flux added to the system due to the inlet flow had a tremendous effect on the mixing of the non-Newtonian fluids exhibiting yield stress.

In addition, the channeling (f) was identified through the dynamic tests with identical operating conditions for the RT, A310, and 3AM impellers and the results are depicted in Figures 8a–c, respectively. The results show that as the power input was raised by increasing the impeller speed, the channeling (f) decreased for all three impellers. At a lower impeller speed, the shear stress produced by the impeller was less than the yield stress of the fluid in the stagnant zone. At a higher impeller speed, the xanthan gum solution was swept away from the impeller, leading to improved mixing by overcoming the fluid yield stress. Thus, it provided less channeling by entraining the feed into the mixing zones. In fact, the channeling (f) should be minimized to enhance the efficiency of the continuous-flow mixing system.

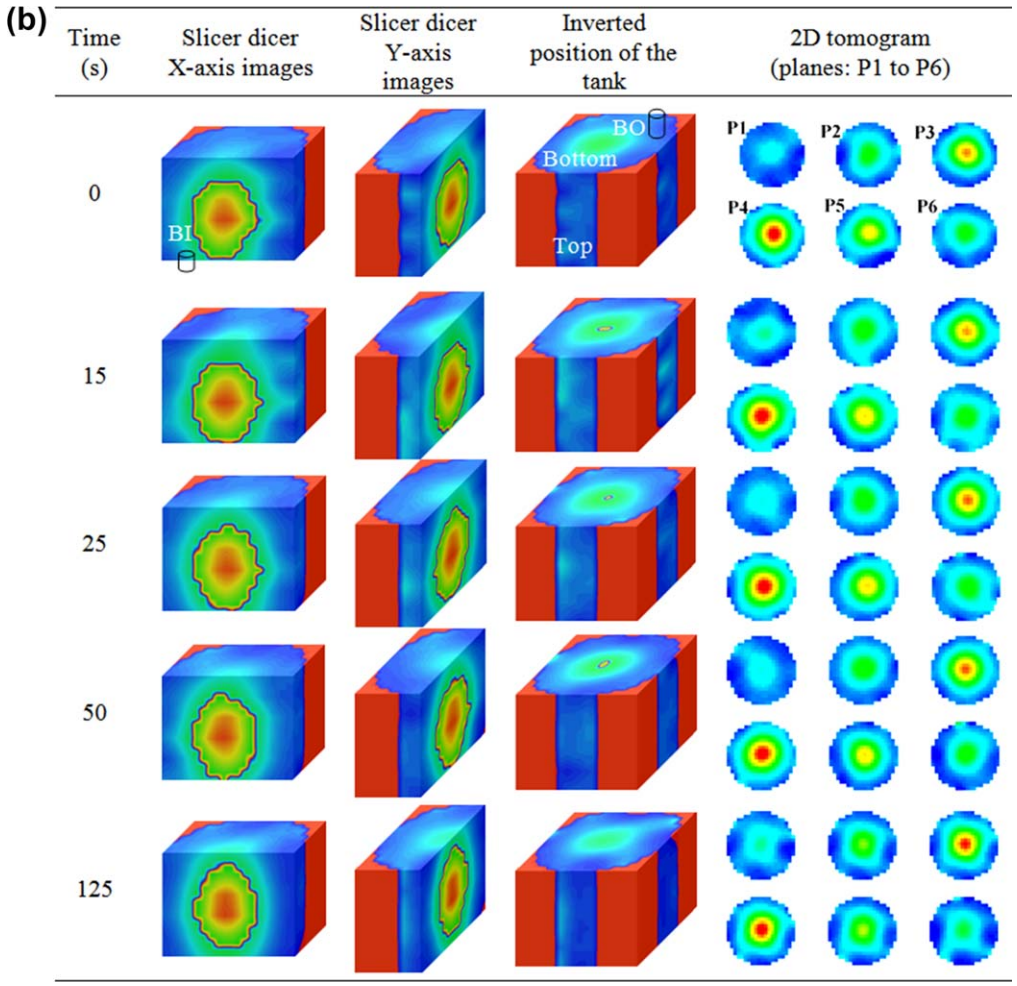

Figure 9. (Continued).

[Color figure can be viewed in the online issue, which is available at wileyonlinelibrary.com.]

The subsequent discussions explain how the input-output flow in continuous-flow mixing affected the cavern formation. As described in the procedure, once the cavern remained unchanged in the batch mode, the feed and discharge pumps were turned on simultaneously. ERT data were collected and 2-D tomography images were generated. As shown in Figure 3, 2-D tomograms were converted into 3-D images and were sliced using the Slicer Dicer software to get insight into what was happening within the mixing vessel. As mentioned earlier, the cavern volume (V_c) was calculated using the cavern diameter (D_c) and the cavern height (H_c) for a cylindrical shape. However, the shape of the deformed cavern was not exactly cylindrical. Therefore, to measure the total volume of the deformed cavern, the cavern was divided into the small cylindrical segments to approximate the volume of the deformed cavern. The cavern volume measured in batch mixing, when the feed and discharge pumps were off, was used as a reference to estimate the increase in cavern volume due to deformation in continuous mode. Error involved in estimating the cavern volume assuming the cylindrical shape was approximately 4%. The images in Figures 9–12 are presented in four columns in a time series (first column from the left: Slicer Dicer X-axis image; second column: Slicer Dicer Y-axis image; third column: Slicer Dicer block for the inverted position of the tank; and fourth column: 2-D tomograms from planes $P1$ to $P6$). In the third column, the Slicer Dicer images of the tank are presented in an inverted position as it is difficult to view the bottom of the tank from the top. In this 3-D image, the upper surface shows the bottom of the tank and the lower surface shows the top of the tank. The locations of the inlet and outlet are also shown in the Slicer Dicer images. The ERT images depicted in the first row in Figures 9–12 were obtained at zero second (i.e., when the cavern size remained unchanged after the injection of the tracer in the batch mode and before the pumps were turned on). The images in the first row at zero second show that there was almost no tracer at the bottom plane $P6$ in the 2-D tomogram and the top surface of the inverted position of the tank. In Figures 9–12, the images in the second, third, fourth, and fifth rows were taken at 15, 25, 50, and 125 s, respectively, after the pumps were turned on in the continuous mode.

To explore the effects of inlet and outlet locations on the deformation of the cavern, four different configurations, namely, (1) TI-BO (top inlet-bottom outlet), (2) BI-BO (bottom inlet-bottom outlet), (3) TI-TO (top inlet-top outlet), and (4) BI-TO (bottom inlet-top outlet) were tested in the continuous mode for the RT impeller at $N = 30$ rpm, $Q = 1.60 \times 10^{-4}$ m^3 s^{-1}, 1.0% xanthan gum, $V_j = 0.317$ m s^{-1}, and the ERT results are depicted in Figures 9a–d, respectively. In

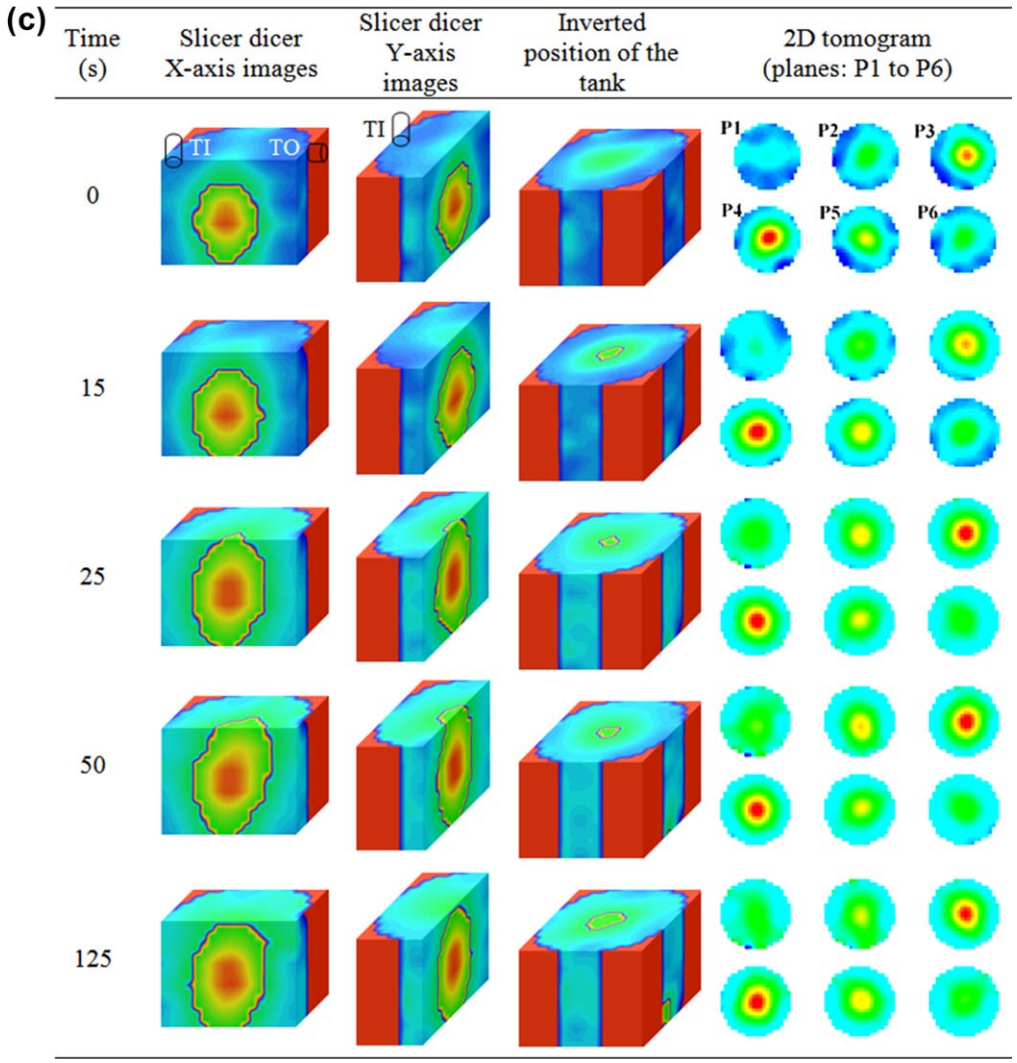

Figure 9. (Continued).

[Color figure can be viewed in the online issue, which is available at wileyonlinelibrary.com.]

the case of the TI-BO configuration (Figure 9a), as the feed and discharge pumps were started simultaneously, images in the second row clearly show that the cavern shape was slightly deformed at the bottom. This was due to the flow of fluid sucked from the BO by the discharge pump. At that moment, the tracer appeared at plane *P*6 in the 2-D tomogram and the top surface of the inverted position of the tank. As time passed, the fresh xanthan gum solution was continuously fed to the tank through the TI, and the mixed solution was drawn from the vessel through the BO. Due to this input-output flow, the cavern shape recorded in the batch mode was deformed in the continuous mode. The concentration of the tracer at the bottom plane *P*6 in the 2-D tomogram and the top surface of the inverted position of the tank increased as shown in subsequent images. It is very clear from the images that the size of the cavern increased as the flow passed through the mixing tank. Finally, the size of the cavern was increased by 11.2% due to the deformation caused by the inlet-outlet flow. This was due to the momentum added to the fluid in the mixing vessel by the input-output flow passing through it. The extra momentum flux added to the fluid in the mixing vessel at the inlet position was about 99.92 Kg m^{-1} s^{-2}.

In the study of the BI-BO configuration as shown in Figure 9b, a small amount of tracer appeared on the bottom plane *P*6 in the 2-D tomogram and on the top surface of the inverted position of the tank in the time series rows 2–4 after the feed and discharge pumps were turned on. In the last row, the tracer disappeared at the bottom of the tank and there was no significant change in the shape of the cavern. The BI-BO configuration was more susceptible to a high degree of channeling and dead volume than the TI-BO configuration. For the BI-BO configuration, the cavern volume increased only by 2.6%. These results show that the extent of the cavern deformation was higher for the TI-BO configuration compared to that for the BI-BO configuration. Patel et al.[20] studied the dynamic performance of the continuous-flow mixing of non-Newtonian fluids in the stirred vessel. They found that the channeling and dead volume were increased by about 5.27 and 5.15%, respectively, when the inlet location was changed from the TI-BO configuration to the BI-BO configuration for the 3AH impeller at 50 rpm. The BI-BO configuration, where both inlet and outlet were located at the bottom of the tank, enabled a large percentage of the feed to be conveyed to the outlet without being drawn into the impeller mixing zone. Therefore, according to the

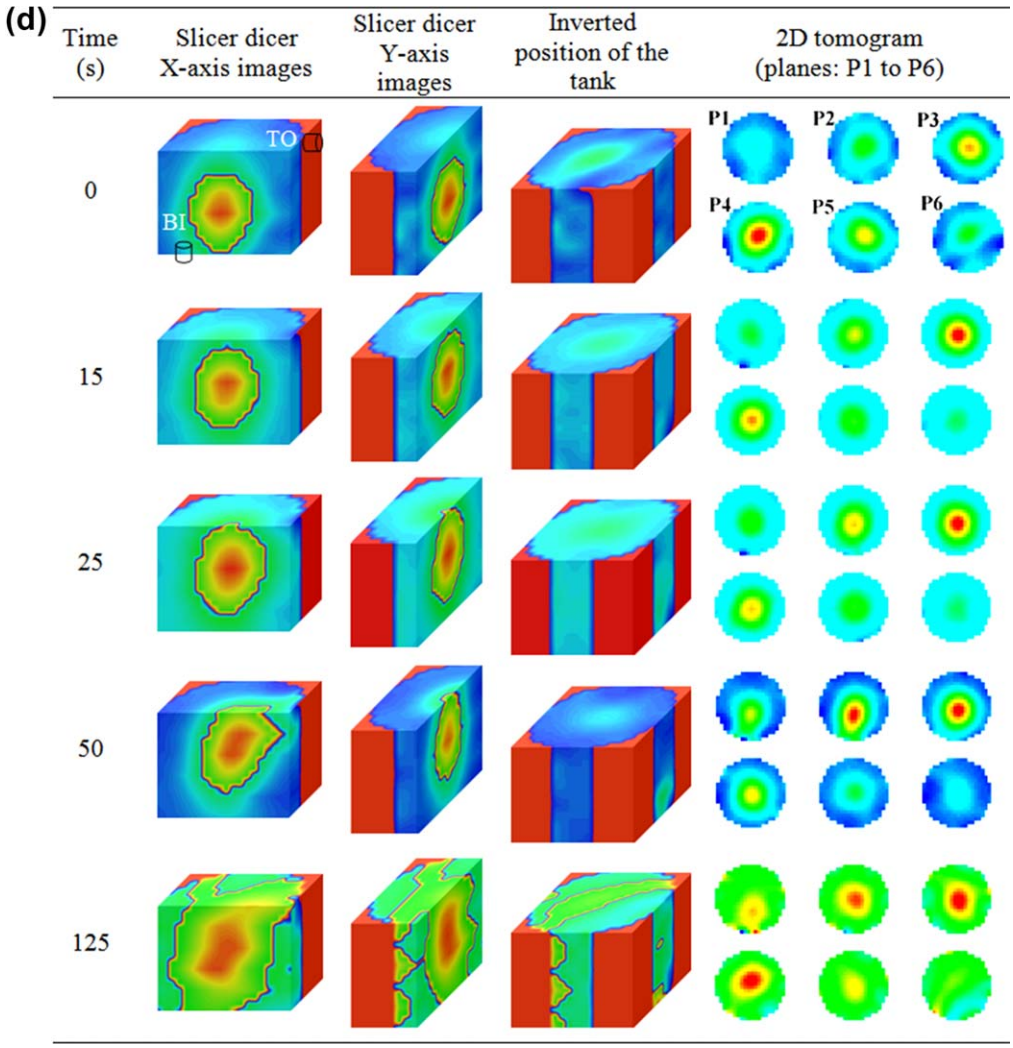

Figure 9. (Continued).

[Color figure can be viewed in the online issue, which is available at wileyonlinelibrary.com.]

cavern deformation depicted in the last row of Figures 9a,b the input-output flow had the least effect on the deformation of the cavern in the BI-BO configuration.

In the TI-TO configuration (Figure 9c), once the feed and discharge pumps were turned on, the cavern shape deformed in such a way that it inclined toward the TO. This was due to the flow of fluid sucked from the TO by the discharge pump. In this configuration, the size of the cavern was increased by about 8% due to the deformation, which was less than that of the TI-BO configuration. According to the deformation of the cavern demonstrated in the last row of Figures 9a,c, it can be seen that the extent of cavern deformation was slightly more in the TI-BO configuration compared to that in the TI-TO configuration. This was due to the fact that the TI-TO configuration enabled a portion of the feed to be channeled directly to the outlet without passing through the impeller mixing zone.

In the BI-TO configuration (Figure 9d), once the feed and discharge pumps were turned on, as shown in the second to fourth rows, initially the whole cavern was slightly pushed from the lower part and shifted toward the upper part of the tank. This was due to the fact that the fresh feed was pumped to the bottom of the tank and this pushed the whole cavern from the lower part of the tank to the upper part of the tank. Simultaneously, the discharge fluid from the mixing tank was drawn from the TO by the discharge pump, which helped the cavern move upwards. Moving toward the last row, the amount of the tracer increased gradually on the top plane $P1$ in the 2-D tomogram and at the top surface of the Slicer Dicer images. The images presented in the last row show that the cavern was completely deformed by the input-output flow and spread over the entire mixing tank in the BI-TO configuration. Eventually, the enlargement of the cavern due to the deformation was about 26.7%. Based on the cavern deformation presented in the last row of Figures 9a–d, the BI-TO configuration was the most effective configuration in deforming the cavern shape rigorously in comparison to the other configurations (TI-BO, BI-BO, and TI-TO). In the case of the BI-TO and TI-BO configurations, the feed was forced to pass through the mixing zone before leaving the vessel. Nevertheless, in the BI-TO configuration, the feed had to face fluid discharge from the impeller and pass through the mixing zone in the direction opposite to the bulk flow within the vessel. Similar results were observed in the study of the dynamic performance of the continuous-flow mixing system in a stirred vessel.[20]

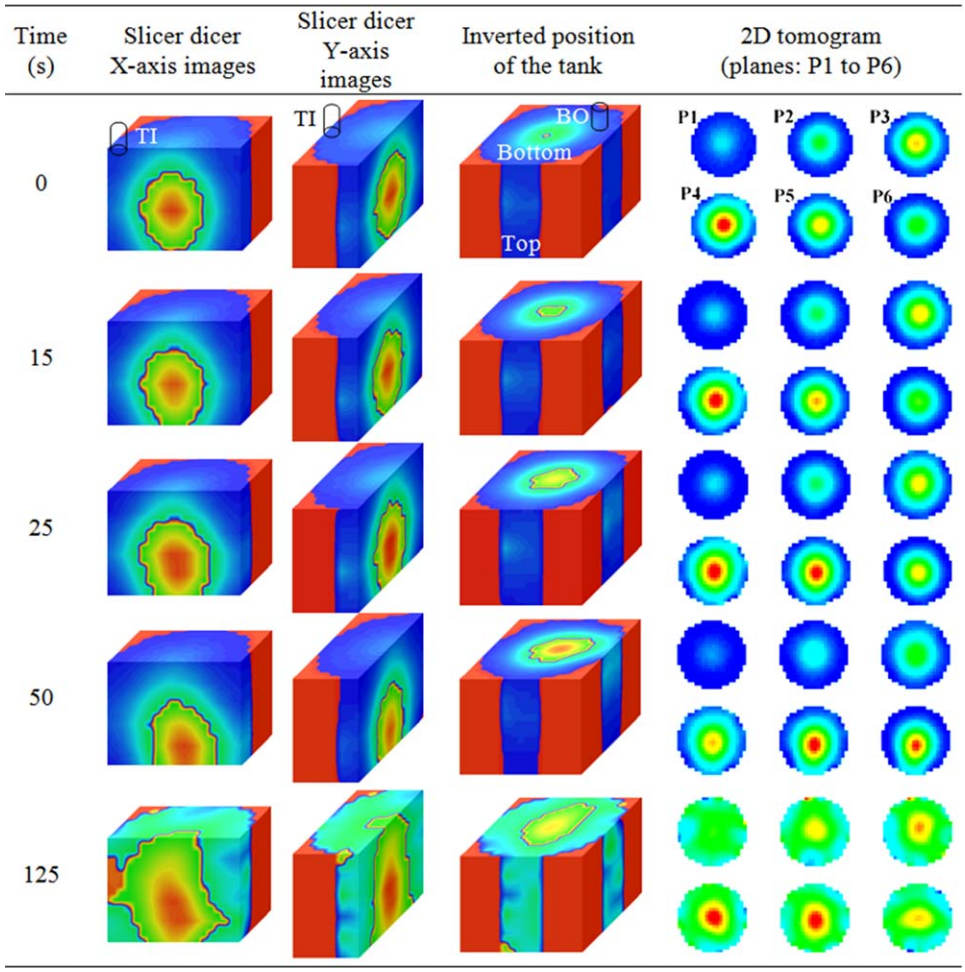

Figure 10. Tomography images obtained for the RT impeller at $N = 30$ rpm, $Q = 1.60 \times 10^{-4}$ m^3 s^{-1}, 0.5% xanthan gum, $V_j = 0.317$ m s^{-1}, and inlet-outlet locations: TI-BO.

[Color figure can be viewed in the online issue, which is available at wileyonlinelibrary.com.]

The fluid rheology significantly affects the performance of the continuous-flow mixing of non-Newtonian fluids. To explore the effect of this parameter, the ERT tests were performed at the same operating conditions as those mentioned in Figure 9a except the xanthan gum concentration. Figure 10 demonstrates the cavern deformation at 0.5% xanthan gum concentration. Once the feed and discharge pumps were turned on, the images in the second row show that the cavern shape was slightly deformed at the bottom due to the discharge of the fluid from the BO. In the subsequent images presented in the time series, the cavern shape got more deformed and higher tracer concentration was detected at the bottom plane *P*6 in the 2-D tomogram and at the top surface of the inverted position of the tank. The ERT images in the last row show that the cavern was completely deformed by the input-output flow and reached the fluid surface and the vessel wall. The size of the cavern was increased by about 21.1% due to the deformation. The images in the last row of Figures 9a and 10 show that the cavern shape was more deformed at the 0.5% xanthan gum solution than at the 1.0% xanthan gum solution. This was due to the fluid yield stress which decreased when the xanthan gum concentration was decreased from 1.0 to 0.5%. The energy dissipation at the lower yield stress is slower than that at the higher yield stress. The fluctuating velocities penetrate quickly in the area outside of the impeller zone at the lower yield stress because of the lesser apparent viscosity of the fluid, which is a function of the fluid yield stress.

The inlet jet velocity (V_j) can also improve the efficiency of the continuous-flow mixing system. To generate a high-velocity jet of the feed in the vessel at the same flow rate, the inlet diameter was reduced. Figure 11 represents the ERT results at the same operating conditions as those mentioned in Figure 9a except the jet velocity, which was $V_j = 1.66$ m s^{-1}. After the feed and discharge pumps were turned on, the images in the second row show that the cavern shape was slightly deformed at the bottom due to the discharge fluid flow from the BO. The successive Slicer Dicer images presented in the second to fourth rows show that the cavern shape at the left hand side was squeezed more compared to the right hand side due to the inlet jet flow. The ERT images in the last row demonstrate that cavern shape was rigorously deformed by the high-velocity jet of the fluid and the cavern volume was increased by about 14.8% due to this deformation. From the images depicted in Figures 9a and 11, it can be seen that as the jet velocity (V_j) was increased from 0.317 to 1.66 m s^{-1}, the deformation of the cavern shape was more noticeable. When an inlet stream is fed into a tank at high velocity, it is expected that the surrounding bulk fluid will be entrained into the feed zone, thus

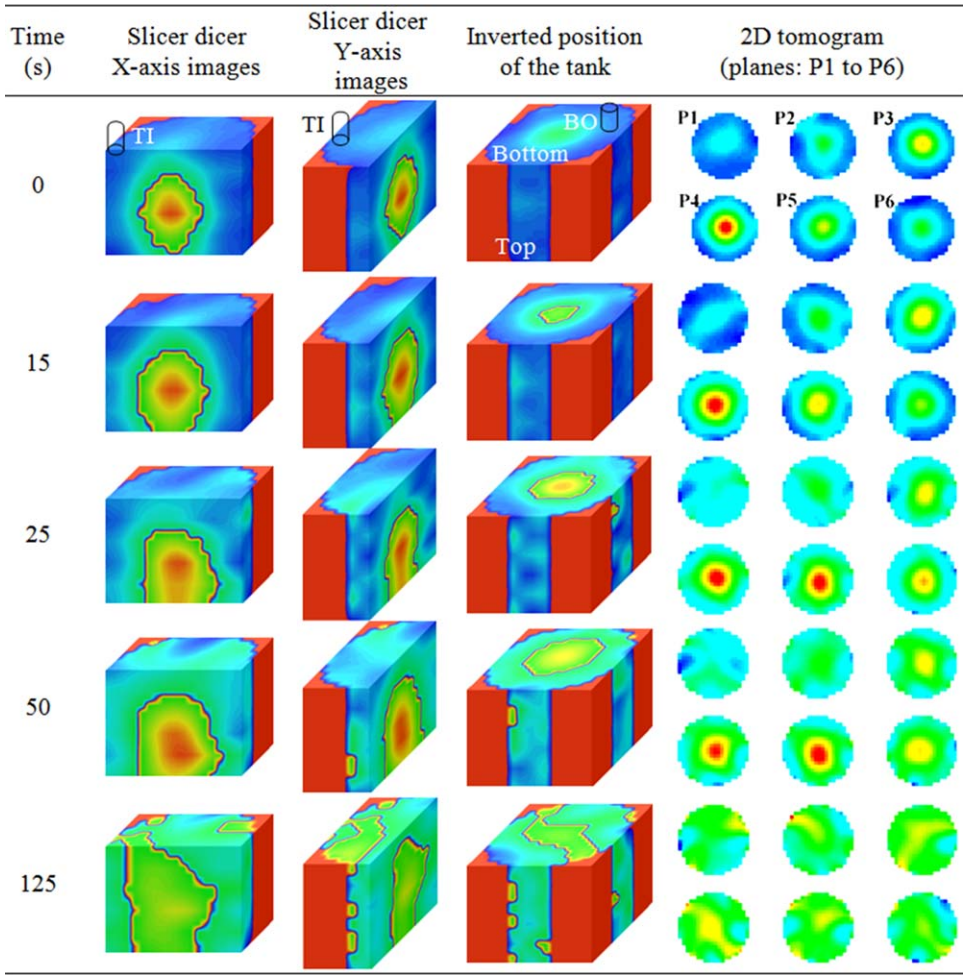

Figure 11. Tomography images obtained for the RT impeller at $N = 30$ rpm, $Q = 1.60 \times 10^{-4}$ m^3 s^{-1}, 1.0% xanthan gum, $V_j = 1.66$ m s^{-1}, and inlet-outlet locations: TI-BO.

[Color figure can be viewed in the online issue, which is available at wileyonlinelibrary.com.]

improving the mixing quality. Moreover, the high-velocity jet of fluid transports the feed promptly to the impeller zone, where it is exposed to high turbulence and is mixed better.[20]

The mixing quality in the continuous-flow mixing system also largely depends on the feed flow rate through the mixing vessel. To study the effects of the feed flow rates on the deformations of the cavern, the ERT tests were conducted at the same operating conditions as those mentioned in Figure 9a except the feed flow rate (Q). Figures 12a,b depict the tomography images for $Q = 5.3 \times 10^{-5}$ m^3 s^{-1} and $Q = 2.36 \times 10^{-4}$ m^3 s^{-1}, respectively. After the feed and discharge pumps were turned on, the images in the second row show that the cavern shape was slightly deformed at the bottom of the tank due to the discharge flow through the BO. Due to the deformation, the cavern volumes increased by nearly 5.6 and 17.7% for $Q = 5.3 \times 10^{-5}$ m^3 s^{-1} and $Q = 2.36 \times 10^{-4}$ m^3 s^{-1}, respectively. From the images demonstrated in the last row of Figures 9a and 12a, it can be observed that the cavern deformation achieved at $Q = 1.60 \times 10^{-4}$ m^3 s^{-1} was more pronounced than that at $Q = 5.3 \times 10^{-5}$ m^3 s^{-1}. Figure 12b shows that the shape of the cavern was deformed severely and the tracer dispersed all around the tank when the feed flow rate was increased to $Q = 2.36 \times 10^{-4}$ m^3 s^{-1}. In fact, the ratio of the Q/Q_{impeller} was employed to study the effect of the feed flow rate on the deformation of the cavern. To calculate Q_{impeller}, an N_Q of 0.72[41,48,49] was chosen for the RT impeller. When the ratio of Q/Q_{impeller} was increased by a factor of three (i.e., Q was increased from 5.3×10^{-5} to 1.60×10^{-4} m^3 s^{-1}), the enlargement of the cavern due to the deformation increased from 5.6 to 11.2%. When the ratio of Q/Q_{impeller} was further increased by a factor of 1.5 (i.e., Q was increased from 1.60×10^{-4} to 2.36×10^{-4} m^3 s^{-1}), the enlargement of the cavern due to the deformation also increased from 11.2 to 17.7%. In addition to this, the quantitative results also show that when the feed flow rate (Q) was increased from 5.3×10^{-5} to 1.60×10^{-4} m^3 s^{-1}, the momentum flux created by the inlet flow increased from 10.99 to 99.92 Kg m^{-1} s^{-2}. When the feed flow rate (Q) was further increased from 1.60×10^{-4} to 2.36×10^{-4} m^3 s^{-1}, the momentum flux generated by the inlet flow also increased from 99.92 to 215.42 Kg m^{-1} s^{-2}. In fact, the extra momentum induced by the input-output flow increased with an increase in the feed flow rate through the mixing tank. Therefore, the deformation of the cavern was more pronounced at the higher flow rate.

Conclusions

ERT was used to measure the cavern volume (V_c) in the mixing of non-Newtonian fluids with yield stress in a batch vessel for the RT, A310, and 3AM impellers. Analysis using

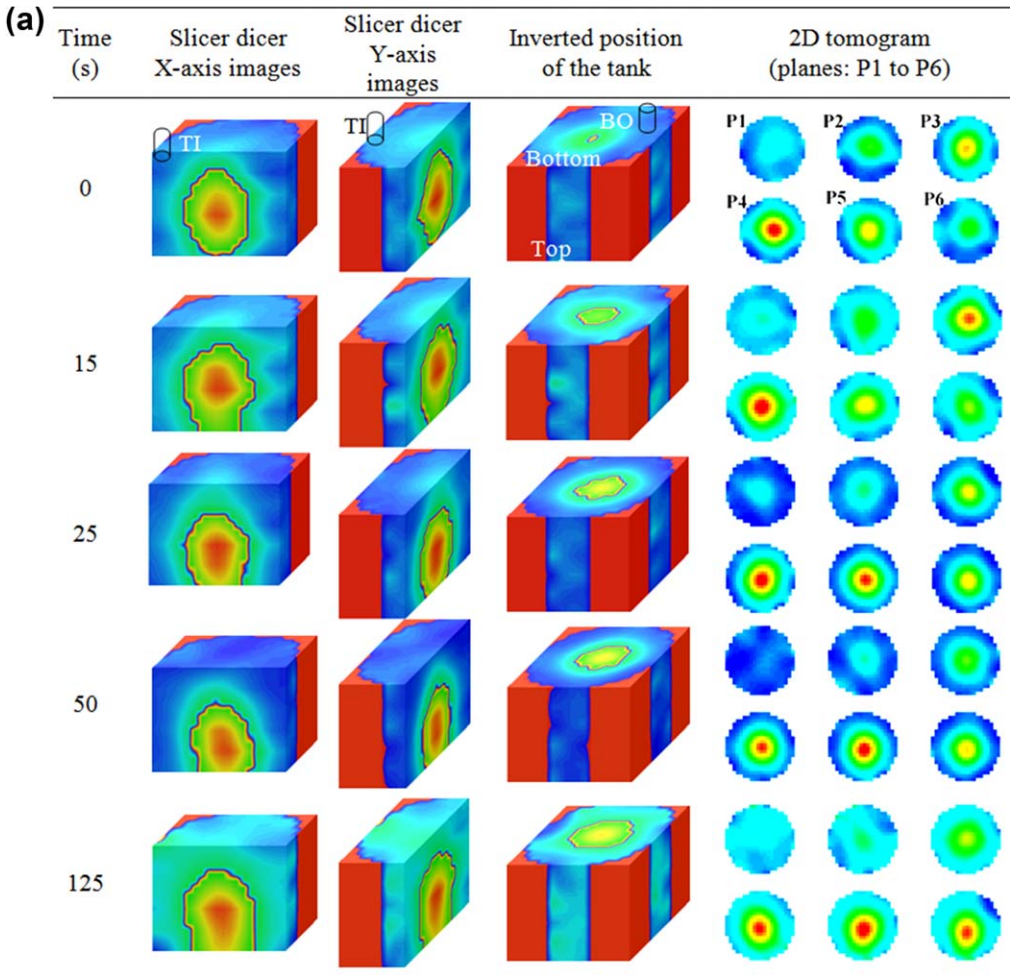

Figure 12. Effect of the feed flow rate on the deformation of the cavern. (a) $Q = 5.3 \times 10^{-5}$ m^3 s^{-1} and (b) $Q = 2.36 \times 10^{-4}$ m^3 s^{-1} (RT impeller, $N = 30$ rpm, 1.0% xanthan gum, and inlet-outlet locations: TI-BO).

[Color figure can be viewed in the online issue, which is available at wileyonlinelibrary.com.]

the 3-D Slicer Dicer images showed that the axial-flow impellers (A310 and 3AM) created taller caverns and higher cavern volumes than those of the radial-flow impeller (RT). Moreover, tests for the cavern volume were carried out for the RT impeller at 0.5, 1.0, and 1.5% xanthan gum concentrations. As the fluid yield stress was decreased by decreasing the fluid concentration, the cavern volume increased. In addition to ERT tests, dynamic tests were performed to estimate the fully mixed volume ($V_{\text{fully mixed}}$) in the continuous-flow mixing system. The cavern volume (V_c) was compared with the fully mixed volume ($V_{\text{fully mixed}}$) for the RT, A310, and 3AM impellers. The results showed that, for the identical operating conditions, the fully mixed volume ($V_{\text{fully mixed}}$) in a continuous-flow mixing vessel was higher than the cavern volume (V_c) in a batch vessel for each impeller used in this study. This was due to the extra momentum induced by the inlet-outlet flow. The extra momentum flux generated by the inlet-outlet flow was estimated and compared with the momentum flux generated by the impeller. These results demonstrated that at a lower impeller speed, the momentum flux added to the system due to the inlet flow had a tremendous effect on the mixing of the non-Newtonian fluids exhibiting yield stress. Moreover, the ratio of the Q/Q_{impeller} was employed to study the effect of the feed flow rate on the deformation of the cavern. When the ratio of Q/Q_{impeller} was increased by a factor of three, the enlargement of the cavern due to the deformation increased from 5.6 to 11.2%. When the ratio of Q/Q_{impeller} was further increased by a factor of 1.5, the enlargement of the cavern due to the deformation also increased from 11.2 to 17.7%.

The ERT system was also employed to visualize the flow of non-Newtonian fluids with yield stress in the continuous-flow mixing system. The effect of the input-output flow on the deformation of the cavern was analyzed using the 2-D tomographic images and the 3-D Slicer Dicer images at different operating conditions and design parameters. The extent of the cavern enlargement due to the extra momentum induced by the input-output flow was estimated for each case. The effect of each factor on the deformation of the cavern is described below:

1. Fluid rheology: The enlargement of the cavern due to the deformation increased from 11.2 to 21.1%, when the fluid yield stress was decreased by reducing the fluid concentration from 1.0 to 0.5%.=

2. Jet effect: When the jet velocity (V_j) was increased from 0.317 to 1.66 m s^{-1}, the enlargement of the cavern due to the deformation increased from 11.2 to 14.8%, and the tracer was dispersed throughout the tank widely.

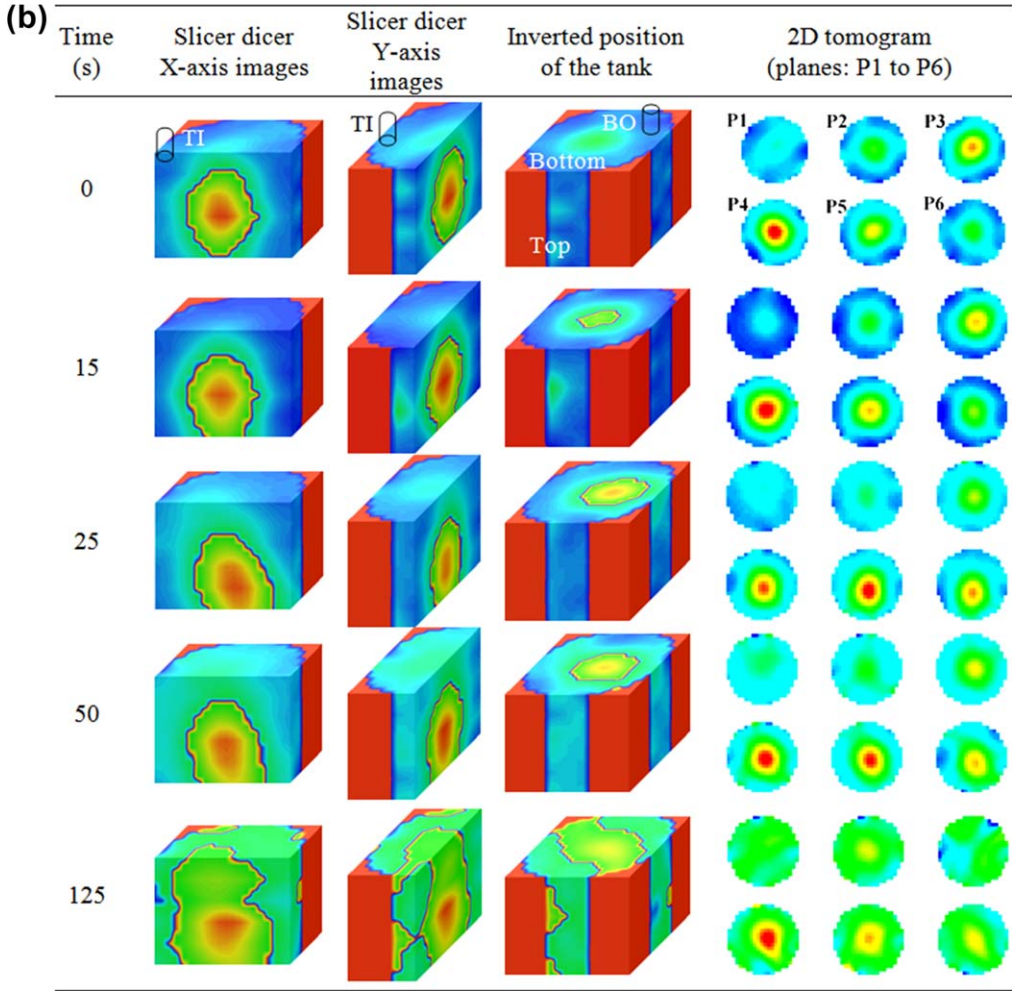

Figure 12. (Continued).

[Color figure can be viewed in the online issue, which is available at wileyonlinelibrary.com.]

3. Feed flow rate: When the feed flow rate (Q) was increased from 5.3×10^{-5} to 2.36×10^{-4} m^3 s^{-1}, the enlargement of the cavern due to the deformation also noticeably increased from 5.6 to 17.7%. The deformation of the cavern was more pronounced at the higher flow rate because of the more momentum flux induced by the input-output flow. In fact, when the feed flow rate (Q) was increased from 5.3×10^{-5} to 2.36×10^{-4} m^3 s^{-1}, the momentum flux added to the system by the inlet flow increased from 10.99 to 215.42 Kg m^{-1} s^{-2}.
4. Inlet and outlet locations: The cavern volume increased by about 2.6, 8.0, 11.2, and 26.7% for BI-BO, TI-TO, TI-BO, and BI-TO, respectively, due to the deformation. The TI-TO and BI-BO configurations enabled the fluid to pass from inlet to outlet without being pushed into the impeller mixing zone, whereas in the BI-TO and TI-BO configurations, the feed was forced to pass through the mixing zone before leaving the vessel.

Acknowledgment

The financial support of the Natural Science and Engineering Research Council of Canada (NSERC, PGS D2), Ontario Graduate Scholarship (OGS), and Ontario Graduate Scholarship in Science and Technology (OGSST) are gratefully acknowledged.

Notation

A = cross section area of the inlet pipe, m^2
A_i = swept area by the impeller, m^2
D = impeller diameter, m
D_c = cavern diameter, m
f = percentage of channeling, fraction
G = transfer function, -
H = fluid height in the vessel, m
H_c = cavern height, m
K = consistency index, Pa s^n
K_s = Metzner-Otto constant, -
M = torque, N m
n = power-law index, -
n_e = number of electrodes, -
N = impeller rotational speed, s^{-1}
N_Q = dimensionless impeller flow number, -
P = power, W
P_o = power number, -
$P1$–$P6$ = plane number, -
Q = volumetric feed flow rate, m^3 s^{-1}
$Q_{impeller}$ = impeller pumping rate, m^3 s^{-1}
R = percentage of recirculation, fraction
Re = Reynolds number, -
Re_y = yield stress Reynolds number, -
r, Φ, z = cylindrical coordinates, m, °, m
T = tank diameter, m

T_1, T_2 = time delay, s
v = velocity of the fluid passing through the inlet, m s^{-1}
V_c = cavern volume, m^3
$V_{\text{fully mixed}}$ = fully mixed volume, m^3
V_j = jet velocity, m s^{-1}
v_{tip} = impeller tip velocity, m s^{-1}
V_{total} = fluid volume inside the mixing tank, m^3

Greek letters

$\dot{\gamma}$ = shear rate, s^{-1}
$\dot{\gamma}_{\text{avg}}$ = average shear rate, s^{-1}
η = = apparent viscosity, Pa s
η_p = impeller pumping efficiency, -
ρ = fluid density, kg m^{-3}
τ_s = shear stress, Pa
τ_1 and τ_2 = time constant, s
τ_y = fluid yield stress, Pa

Literature Cited

1. Wichterle K, Wein O. Agitation of concentrated suspensions. Paper presented at: CHISA' 75, Prague, Czechoslovakia, 1975:Paper B4.6.
2. Solomon J, Elson TP, Nienow AW. Cavern sizes in agitated fluids with a yield stress. *Chem Eng Commun.* 1981;11:143–164.
3. Elson TP, Cheesman DJ. X-ray studies of cavern sizes and mixing performance with fluids possessing a yield stress. *Chem Eng Sci.* 1986;41(10):2555–2562.
4. Elson TP. Mixing of fluids possessing a yield stress. In: Proceedings of the 6th European Conference on Mixing. Pavia, Italy: AIDIC-Associazione Italian di Ingegeneria Chemica, 1988:485–492.
5. Amanullah A, Hjorth SA, Nienow AW. A new mathematical model to predict cavern diameters in highly shear thinning, power law liquids using axial flow impellers. *Chem Eng Sci.* 1998;53(3):455–469.
6. Wilkens RJ, Miller JD, Dietz DC, Myers KJ. New technique for measuring and modeling cavern dimensions in a Bingham plastic fluid. *Chem Eng Sci.* 2005;60:5269–5275.
7. Hirata Y, Aoshima Y. Formation and growth of cavern in yield stress fluids agitated under baffled and non-Newtonian conditions. *Chem Eng Res Des.* 1996;74(4):438–444.
8. Hui LK, Bennington CPJ, Dumont GA. Cavern formation in pulp suspensions using side-entering axial-flow impellers. *Chem Eng Sci.* 2009;64:509–519.
9. Pakzad L, Ein-Mozaffari F, Chan P. Using electrical resistance tomography and computational fluid dynamics modeling to study the formation of cavern in the mixing of pseudoplastic fluids possessing yield stress. *Chem Eng Sci.* 2008;63(9):2508–2522.
10. Saeed S, Ein-Mozaffari F, Upreti SR. Using computational fluid dynamics to study the dynamic behavior of the continuous mixing of Herschel-Bulkley Fluids. *Ind Eng Chem Res.* 2008;47:7465–7475.
11. Ein-Mozaffari F, Bennington CPJ, Dumont GA. Suspension yield stress and the dynamic response of agitated pulp chests. *Chem Eng Sci.* 2005;60:2399–2408.
12. Mavros P, Naude I, Xuereb C, Bertrand J. Laser Doppler velocimetry in agitated vessels: Effect of continuous liquid stream on flow patterns. *Chem Eng Res Des.* 1997;75(A):763–776.
13. Mavros P, Xuereb C, Fort I, Bertrand J. Investigation by laser Doppler velocimetry of the effects of liquid flow rates and feed positions on the flow patterns induced in a stirred tank by an axial-flow impeller. *Chem Eng Sci.* 2002;57:3939–3952.
14. Mavros P, Xuereb C, Fort I, Bertrand J. Investigation of flow patterns in continuous-flow stirred vessels by laser Doppler velocimetry. *Can J Chem Eng.* 2002;80:591–600.
15. Roussinova V, Kresta SM. Comparison of continuous blend time and residence time distribution models for a stirred tank. *Ind Eng Chem Res.* 2008;47(10):3532–3539.
16. Samaras K, Mavros P, Zamboulis D. Effect of continuous stream and agitator type on CFSTR mixing state. *Ind Eng Chem Res.* 2006;45:4805–4815.
17. Aubin J, Kresta, SM, Bertrand J, Xuereb C, Fletcher DF. Alternate operating methods for improving the performance of continuous stirred tank reactors. *Chem Eng Res Des.* 2006;84(A7):569–582.
18. Khopkar AR, Mavros P, Ranade VV, Bertrand J. Simulation of flow generated by an axial flow impeller - batch and continuous operation. *Chem Eng Res Des.* 2004;82(A6):737–751.
19. Ford C, Ein-Mozaffari F, Bennington CPJ, Taghipour, F. Simulation of mixing dynamics in agitated pulp stock chests using CFD. *AIChE J.* 2006;52(10):3562–3569.
20. Patel D, Ein-Mozaffari F, Mehrvar M. Dynamic performance of continuous-flow mixing of pseudoplastic fluids exhibiting yield stress in stirred reactors. *Ind Eng Chem Res.* 2011;50(15):9377–9389.
21. Ein-Mozaffari F, Dumont GA, Bennington CPJ. Performance and design of agitated pulp stock chests. *Appita J.* 2003;56(2):127–133.
22. Patel D, Ein-Mozaffari F, Mehrvar M. Improving the dynamic performance of continuous-flow mixing of pseudoplastic fluids possessing yield stress using Maxblend impeller. *Chem Eng Res Des.* 2012;90(4):514–523.
23. Ein-Mozaffari F, Bennington CPJ, Dumont GA. Optimization of rectangular pulp stock mixing chest dimensions using dynamic tests. *Tappi J.* 2007;6(2):24–30.
24. Patel D, Ein-Mozaffari F, Mehrvar M. Effect of impeller type on continuous-flow mixing of non-Newtonian fluids in stirred vessels through dynamic tests. *Can J Chem Eng.* 2012;90(2):290–298.
25. Saeed S, Ein-Mozaffari F. Using dynamic tests to study the continuous mixing of xanthan gum solutions. *J Chem Technol Biotechnol.* 2008;83:559–568.
26. Patel D, Ein-Mozaffari F, Mehrvar M. Characterization of the continuous-flow mixing of non-Newtonian fluids using the ratio of residence time to batch mixing time. *Chem Eng Res Des.* 2013;91(7):1223–1234.
27. Ein-Mozaffari F, Kammer LC, Dumont GA, Bennington CPJ. The effect of operating conditions and design parameters on the dynamic behaviour of agitated pulp stock chests. *Can J Chem Eng.* 2004;82(1):154–161.
28. Kammer LC, Ein-Mozaffari F, Dumont GA, Bennington CPJ. Identification of channeling and recirculation parameters of agitated pulp stock chests. *J Process Control.* 2005;15(1):31–38.
29. Ein-Mozaffari F, Kammer LC, Dumont GA, Bennington CPJ. Dynamic modeling of agitated stock chests. *Tappi J.* 2003;2:13–17.
30. Herschel WE, Bulkley R. Measurements of consistency as applied to rubber-benzene solutions. *Proc Am Soc Test Mater.* 1926;26(2):621–633.
31. Boden S, Bieberle M, Hampel U. Quantitative measurement of gas hold-up distribution in a stirred chemical reactor using x-ray cone-beam computed tomography. *Chem Eng J.* 2008;139(2):351–362.
32. Ford JJ, Heindel TJ, Jensen TC, Drake JB. X-ray computed tomography of a gas-sparged stirred-tank reactor. *Chem Eng Sci.* 2008;63:2075–2085.
33. Liu Y-J, Li W, Han L-C, Cao Y, Luo H-A, Al-Dahhan M, Dudukovic MP. γ-CT measurement and CFD simulation of cross section gas holdup distribution in a gas–liquid stirred standard Rushton tank. *Chem Eng Sci.* 2011;66(17):3721–3731.
34. Thatte AR, Ghadge RS, Patwardhan AW, Joshi JB, Singh G. Local gas holdup measurement in sparged and aerated tanks by γ -ray attenuation technique. *Ind Eng Chem Res.* 2004;43(17):5389–5399.
35. Hosseini S, Patel D, Ein-Mozaffari F, Mehrvar M. Study of solid-liquid mixing in agitated tanks through electrical resistance tomography. *Chem Eng Sci.* 2010;65(4):1374–1384.
36. Hosseini S, Patel D, Ein-Mozaffari F, Mehrvar M. Study of solid-liquid mixing in agitated tanks through computational fluid dynamics modeling. *Ind Eng Chem Res.* 2010;49(9):4426–4435.
37. Patel D, Ein-Mozaffari F, Mehrvar M. Using tomography to characterize the mixing of non-Newtonian fluids with a Maxblend impeller. *Chem Eng Technol.* 2013;36(4):687–695.
38. Barber CD, Brown BH, Freeston IL. Imaging spatial distributions of resistivity using applied potential tomography. *Electron Lett.* 1983;19:933–935.
39. Barber CD, Brown BH. Applied potential tomography. *J Phys E Sci Instrum.* 1984;17(9):723–733.
40. Metzner AB, Otto RE. Agitation of non-Newtonian fluids. *AIChE J.* 1957;3(1):3–11.
41. Paul EL, Atiemo-Obeng VA, Kresta SM. Handbook of Industrial Mixing: Science and Practice. New Jersey, Hoboken: Wiley, 2004.
42. Chhabra RP, Richardson JF. Non-Newtonian Flow and Applied Rheology, Engineering Application, 2nd ed. Amsterdam: Elsevier, Butterworth-Heinemann, 2008.
43. Holden PJ, Wang M, Mann R, Dickin FJ, Edward RB. Imaging stirred-vessel macromixing using electrical resistance tomography. *AIChE J.* 1998;44(4):780–790.
44. Galindo E, Nienow AW. Mixing of highly viscous simulated xanthan fermentation broths with the Lightnin A-315 impeller. *Biotechnol Prog.* 1992;8(3):223–239.

45. Amanullah A, Hjorth SA, Nienow AW. Cavern sizes generated in highly shear thinning viscous fluids by SCABA 3SHP1 impellers. *Food Bioprod Process.* 1997;75(4):232–238.

46. Uhl VW, Gray JB. Mixing, Theory and Practice, Vol. 1. New York, NY: Academic Press, 1996.

47. Saeed S. Dynamic and CFD Modeling of a Continuous-Flow Mixer Using Fluids with Yield Stress. MASc Thesis, Toronto, ON, Canada: Ryerson University, 2007.

48. Weetman RJ, Oldshue JY. Power, flow and shear characteristics of mixing impellers. In: the Proceedings of the 6th European Conference on Mixing, Italy, Cranfield, UK: AIDIC/BHR Group, 1988:43–50.

49. Nienow AW. Hydrodynamics of stirred bioreactors. *Appl Mech Rev*. 1998;51(1):3–32.

Manuscript received Sept. 15, 2012, revision received Apr. 25, 2013, and final revision received Sept. 15, 2013.